

Fingering instability down the outside of a vertical cylinder

Linda B. Smolka^{1,a)} and Marc SeGall^{1,2,b)}

¹Department of Mathematics, Bucknell University, Lewisburg, Pennsylvania 17837, USA

²Department of Physics, Bucknell University, Lewisburg, Pennsylvania 17837, USA

(Received 23 June 2011; accepted 27 July 2011; published online 19 September 2011)

We present an experimental and numerical study examining the dynamics of a gravity-driven contact line of a thin viscous film traveling down the outside of a vertical cylinder of radius R . Experiments on cylinders with radii ranging between 0.159 and 3.81 cm show that the contact line is unstable to a fingering pattern for two fluids with differing viscosities, surface tensions, and wetting properties. The dynamics of the contact line is studied and results are compared to previous studies of inclined plane experiments in order to understand the influence substrate curvature plays on the fingering pattern. A lubrication model is derived for the film height in the limit that $\epsilon = H/R \ll 1$, where H is the upstream film thickness, and in terms of a Bond number $\rho g R^3 / (\gamma H)$, and the linear stability of the contact line is analyzed using traveling wave solutions. Curvature controls the capillary ridge height of the traveling wave and the range of unstable wavelength when $\epsilon = O(10^{-1})$, whereas the shape and stability of the contact line converge to the behavior one observes on a vertical plane when $\epsilon \leq O(10^{-2})$. The most unstable wave mode, cutoff wave mode for neutral stability, and maximum growth rate scale as $\widehat{\text{Bo}}^{0.45}$ where $\widehat{\text{Bo}} = \rho g R^2 / \gamma \geq 1.3$, and the contact line is unstable to fingering when $\widehat{\text{Bo}} \geq 0.56$. Using the experimental data to extrapolate outside the range of validity of the thin film model, we estimate the contact line is stable when $\widehat{\text{Bo}} < 0.56$. Agreement is excellent between the model and the experimental data for the wave number (i.e., number of fingers) and wavelength of the fingering pattern that forms along the contact line. © 2011 American Institute of Physics. [doi:10.1063/1.3633530]

I. INTRODUCTION

The dynamics of thin fluid layers spreading on solid substrates has applications ranging from coating processes in manufacturing (applying paints, fabricating semiconductors, and coating medications) to geological processes (lava flow). Typically, in manufacturing applications, a uniform coating is desired with no dry patches. In the presence of external forcing, such as gravitational,^{1,2} centrifugal³ or Marangoni,^{4,5} the moving contact line located at the fluid/solid/air interface can become unstable to undulatory perturbations that evolve into fingers. The capillary ridge that forms along the advancing contact line plays a significant role in the fingering pattern that emerges⁶ and the wetting property of the fluid plays a key role in controlling film coverage.² A recent review by Craster and Matar⁷ highlights the advances and challenges ahead in understanding the dynamics of thin film flows in these and in other settings. Our study focuses on the dynamics of a gravity-driven contact line of a thin film flowing down the outside of a vertical cylinder which has applications to the coating of cylinders ranging in size from fibers to conduits.

Numerous experimental and analytical studies have examined the dynamics of a gravity-driven contact line down an inclined or vertical plane,^{1,2,6,8–27} while other studies have examined the dynamics of thin films down the outside of a horizontal cylinder and spherical substrate³⁵ and on

the inside or outside of a cylindrical substrate after the substrate has been fully coated.^{28–34} Flow down the outside of a vertical cylinder of radius R introduces two effects that distinguish it from the planar case: azimuthal curvature and periodic boundary conditions. Within this context, interesting questions arise that probe the effects of curvature, including

1. Given that azimuthal curvature becomes negligible as $R \rightarrow \infty$, is there a critical radius R_c above which the contact line behavior becomes indistinguishable from that on a vertical plane?
2. Is there a critical radius r_c below which fingering is inhibited? Determining the optimal cylinder size that reduces finger formation for a specific fluid could be useful in coating processes.
3. How do features of the fingering pattern, such as finger shape, growth, and wavelength, depend on the azimuthal curvature and fluid properties? To understand curvature's influence, we compare these quantities to values reported in experimental and numerical studies for the planar case.

Given the connection between a cylindrical and planar substrate, we highlight results from experimental and numerical studies on inclined and vertical planes.

The motion of a gravity-driven contact line down an inclined plane has been examined experimentally for viscous,^{1,2,6,9–13} particle-laden,¹⁴ and yield-stress fluids¹⁵ and for granular media¹⁶ (avalanches). For viscous fluids, several experimental studies have focused on the shape, wavelength, and growth of the fingering pattern that forms under constant volume^{1,2,9–12} or constant flux⁶ conditions using both wetting and partially wetting fluids. For inclination angles up to 54°,

^{a)}Electronic mail: lsmolka@bucknell.edu.

^{b)}Present address: CREOL, University of Central Florida, Orlando, FL 32816, USA.

Huppert¹ found glycerin forms long straight fingers of uniform width with the tip positions scaling like $t^{0.6}$ while the trough positions remain stationary. In contrast, he found that silicone oil fingers form a triangular sawtooth pattern with tip and trough positions scaling like $t^{0.35}$ and $t^{0.28}$, respectively.¹ Jerret and de Bruyn¹⁰ found the mean position of the glycerin tips scale like $t^{0.65}$ for inclination angles as large as 32° . Planar studies have focused on how inclination angle effects the fingering pattern. A goal of this study is to understand how curvature of the cylindrical substrate effects the fingering pattern. Experiments are conducted with the same fluids used in inclined plane studies^{1,2,9,10} in order to draw comparisons and to distinguish curvature's effect on the flow.

Lubrication theory is commonly used to model thin film flows where the fluid motion is averaged over the film depth. The lubrication model for a thin film of height $x = h(z, y, t)$ flowing down a vertical plane is given by

$$\partial_t h + \partial_z h^3 + \nabla \cdot (h^3 \nabla \nabla^2 h) = 0, \quad (1)$$

where y is the transverse direction, z is parallel to the direction of gravity, and the evolution of the film height is controlled by gravitational (second term) and surface tension effects (third term).^{17–19} Hydrodynamic modeling breaks down at a moving contact line as the no-slip condition causes a stress singularity at the fluid/solid/air interface.³⁶ To regularize this problem, the no-slip condition is relaxed by allowing slip at the contact line^{37,38} or introducing a thin precursor film ahead of the contact line.¹⁹ Both models require introducing a free parameter into the problem, either a slip parameter or a precursor film thickness; Spaid and Homsy²⁰ show qualitatively similar stability results that are obtained when these two parameters are equal in value. In a numerical study, Diez *et al.*²⁴ find the precursor model is computationally more efficient than the slip model.

In a linear stability analysis of flow down a vertical plane using Eq. (1), Troian *et al.*¹⁹ show the contact line is unstable to a finite band of wavenumbers and that short wavelength perturbations are stabilized by surface tension; these results were found to be weakly dependent on the precursor film thickness. In a similar analysis, Spaid and Homsy²⁰ show the most unstable wave number is insensitive to the precursor thickness while the maximum growth rate is weakly sensitive. Predictions for the most unstable wavelength by Troian *et al.*¹⁹ were found to agree well with experimental observations of Huppert¹ and Jerret and de Bruyn.¹⁰ Bertozzi and Brenner⁸ extended the analysis of Troian *et al.* to an inclined plane and found that the normal component of gravity reduces the unstable growth rates. Several studies have examined the influence of perturbations within the precursor film on contact line stability.^{8,13,21}

Computational studies of viscous flow down inclined or vertical planes using a lubrication model for partial and complete wetting fluids have investigated short- and long-time dynamics of the contact line^{18,22,23,26} and have been instrumental in identifying the primary factors that control the nonlinear dynamics of finger formation on planar surfaces. In early work, Schwartz¹⁸ examined finger formation for completely wetting fluids using a precursor film model.

Moyle *et al.*²² using a slip model find that the contact slope is a key ingredient to accurately model film coverage and finger shape for partially and completely wetting fluids. Eres *et al.*²³ use a disjoining pressure model, which incorporates a precursor film layer and static contact angle, to model partially wetting fluids. Their predictions of finger wavelength and growth rate agree with linear stability results and three regimes of fingering pattern were identified as a function of the contact angle. Finally, Kondic and Diez²⁶ have examined the influence of inclination angle on finger shape for completely wetting fluids.

The outline of the paper is as follows. In Sec. II, an evolution equation for film height that models the gravity-driven flow of a viscous film down the outside of a vertical cylinder is derived using lubrication theory. In Sec. III, experimental data for two fluids and six cylinders ($0.159 \leq R \leq 3.18$ cm) is presented. In Sec. IV, the unperturbed contact line is modeled by an axisymmetric traveling wave solution, the linear stability of the traveling wave is analyzed to perturbations in the azimuthal direction, and predictions from the model are compared to experimental data. Conclusions are provided in Sec. V.

II. DERIVATION OF LUBRICATION MODEL

An incompressible Newtonian fluid, of kinematic viscosity ν , density ρ , and surface tension γ , flows under gravity down the outside of a vertical cylinder of radius R (see Fig. 1); the acceleration of gravity is denoted by g . The flow, described in cylindrical coordinates with axial coordinate z directed down along the cylinder axis, has velocity field $\mathbf{u} = (u, v, w)$ and pressure field p with free surface h measured radially from the cylinder surface as shown in Fig. 1; the mean curvature of the free surface is denoted by κ . For convenience, a modified radial coordinate $y = r - R$ is introduced so that the flow can be analyzed in the interval $0 < y < h$, with $y = 0$ corresponding to the cylinder surface and $y = h$ to the free surface.

In experiments, we have investigated the flow of fluid down the outside of a vertical cylinder for a range of cylinder radii ($0.159 \leq R \leq 3.81$ cm). For all but the smallest

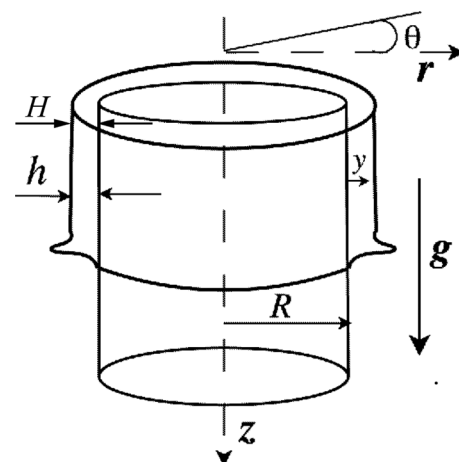


FIG. 1. Schematic of a viscous film of thickness $h(\theta, z, t)$ flowing down the outside of a vertical cylinder of radius R .

cylinder, the quasi-steady film thickness behind the contact line, H (shown in Fig. 1), was significantly smaller than the cylinder radius. We make use of this observation by deriving a lubrication model in the limit that $\epsilon = H/R \ll 1$; notice ϵ is proportional to the substrate curvature. Our presentation closely matches the derivation by Evans *et al.*,³⁰ though the direction of the flow and orientation of the experiment they examine are different than those considered here. Following Evans *et al.*,³⁰ the free boundary problem is nondimensionalized with the film thickness scaled by H and the substrate dimensions by R

$$\bar{y} = \frac{y}{\epsilon R}, \quad \bar{h} = \frac{h}{\epsilon R}, \quad \bar{z} = \frac{z}{R}, \quad \bar{r} = \frac{r}{R}, \quad \bar{t} = \frac{t}{\mathbb{T}}, \quad (2a)$$

$$\bar{u} = \frac{u}{\epsilon \mathbb{U}}, \quad \bar{v} = \frac{v}{\mathbb{U}}, \quad \bar{w} = \frac{w}{\mathbb{U}}, \quad \bar{p} = \frac{p}{\mathbb{P}}, \quad \bar{\kappa} = R\kappa, \quad (2b)$$

where the overbar denotes dimensionless quantities, t denotes time, and the characteristic velocity, pressure, and time scales are $\mathbb{U} = gH^2/\nu$, $\mathbb{P} = \rho gH$, and $\mathbb{T} = R/\mathbb{U}$, respectively. Note that the pressure and time scales were chosen to obtain a lubrication approximation,³⁰ and the scaled radius can be written as $\bar{r} = 1 + \epsilon \bar{y}$.

Using these scalings, the nondimensional form of the continuity equation and Navier-Stokes equations which govern the flow are

$$\frac{1}{\bar{r}} \partial_{\bar{y}}(\bar{r}\bar{u}) + \frac{1}{\bar{r}} \partial_{\theta} \bar{v} + \partial_{\bar{z}} \bar{w} = 0, \quad (3a)$$

$$\begin{aligned} \epsilon^2 \text{Re} \left(\epsilon \partial_{\bar{t}} \bar{u} + \epsilon \bar{u} \partial_{\bar{y}} \bar{u} + \epsilon \frac{\bar{v}}{\bar{r}} \partial_{\theta} \bar{u} + \epsilon \bar{w} \partial_{\bar{z}} \bar{u} - \frac{\bar{v}^2}{\bar{r}} \right) \\ = -\partial_{\bar{y}} \bar{p} + \epsilon \bar{\Delta} u - \epsilon^3 \frac{\bar{u}}{\bar{r}^2} - \frac{2\epsilon^2}{\bar{r}^2} \partial_{\theta} \bar{v}, \end{aligned} \quad (3b)$$

$$\begin{aligned} \epsilon^2 \text{Re} \left(\partial_{\bar{t}} \bar{v} + \bar{u} \partial_{\bar{y}} \bar{v} + \frac{\bar{v}}{\bar{r}} \partial_{\theta} \bar{v} + \bar{w} \partial_{\bar{z}} \bar{v} + \epsilon \frac{\bar{u}\bar{v}}{\bar{r}} \right) \\ = -\frac{\epsilon}{\bar{r}} \partial_{\theta} \bar{p} + \bar{\Delta} v - \epsilon^2 \frac{\bar{v}}{\bar{r}^2} + \frac{2\epsilon^3}{\bar{r}^2} \partial_{\theta} \bar{u}, \end{aligned} \quad (3c)$$

$$\epsilon^2 \text{Re} \left(\partial_{\bar{t}} \bar{w} + \bar{u} \partial_{\bar{y}} \bar{w} + \frac{\bar{v}}{\bar{r}} \partial_{\theta} \bar{w} + \bar{w} \partial_{\bar{z}} \bar{w} \right) = -\epsilon \partial_{\bar{z}} \bar{p} + \bar{\Delta} w + 1, \quad (3d)$$

where the choice of scaling for the radial velocity ensures all terms in Eq. (3a) are $O(1)$, $\text{Re} = R\mathbb{U}/\nu$ is the Reynolds number, $\epsilon^2 \text{Re}$ represents a reduced Reynolds number, and

$$\bar{\Delta} = \frac{1}{\bar{r}} \partial_{\bar{y}}(\bar{r} \partial_{\bar{y}}) + \frac{\epsilon^2}{\bar{r}^2} \partial_{\theta\theta} + \epsilon^2 \partial_{\bar{z}\bar{z}}.$$

Using lubrication theory, we neglect inertial effects by assuming terms of $O(\epsilon^2 \text{Re})$ and higher are small in Eqs. (3b)–(3d).

The scaled boundary conditions of the flow, include no-slip at the cylinder surface, $\bar{\mathbf{u}} = \mathbf{0}$ at $\bar{y} = 0$, and the normal stress, tangential stress, and kinematic conditions at the free surface $\bar{y} = \bar{h}$, which expanded in ϵ are

$$\begin{aligned} -\bar{p} + 2\epsilon \partial_{\bar{y}} \bar{u} - 2\epsilon \partial_{\bar{z}} \bar{h} \partial_{\bar{y}} \bar{w} - 2\epsilon \partial_{\theta} \bar{h} \partial_{\bar{y}} \bar{v} + O(\epsilon^2) \\ = -\frac{1}{\epsilon \text{Bo}} (1 - \epsilon \bar{h} - \epsilon \bar{\nabla}^2 \bar{h} + O(\epsilon^2)), \end{aligned} \quad (3e)$$

$$\partial_{\bar{y}} \bar{v} - \epsilon \bar{v} + O(\epsilon^2) = 0, \quad (3f)$$

$$\partial_{\bar{y}} \bar{w} + O(\epsilon^2) = 0, \quad (3g)$$

$$\partial_{\bar{t}} \bar{h} + \frac{\bar{v}}{\bar{r}} \partial_{\theta} \bar{h} + \bar{w} \partial_{\bar{z}} \bar{h} = \bar{u}, \quad (3h)$$

where $\bar{\nabla}^2 = \partial_{\theta\theta} + \partial_{\bar{z}\bar{z}}$ and $\widehat{\text{Bo}} = \rho g R^2 / \gamma = (R/l_c)^2$ is the Bond number with $l_c = \sqrt{\gamma/(\rho g)}$ representing the capillary length. The Bond number is related to the reduced Bond number, $\text{Bo} = \epsilon^2 \widehat{\text{Bo}} = \rho g H^2 / \gamma$, used in modeling gravity-driven thin film flow on a planar substrate.¹⁹

Next, we expand the pressure and velocity fields in powers of ϵ

$$\begin{aligned} \bar{p} &= \epsilon^{-1} p_0 + p^{(0)} + \epsilon p^{(1)} + \dots, \\ \bar{\mathbf{u}} &= \mathbf{u}^{(0)} + \epsilon \mathbf{u}^{(1)} + \dots, \end{aligned}$$

where the term $\epsilon^{-1} p_0$ with $p_0 = \widehat{\text{Bo}}^{-1}$ in \bar{p} balances the curvature of the cylindrical substrate in Eq. (3e). Linearizing Eq. (3) in ϵ and solving for \bar{p} and \mathbf{u} , we find at leading order

$$p^{(0)}(\bar{y}, \theta, \bar{z}, \bar{t}) = -\frac{1}{\widehat{\text{Bo}}} (\bar{h} + \bar{\nabla}^2 \bar{h}), \quad (4a)$$

$$\begin{aligned} \mathbf{u}^{(0)}(\bar{y}, \theta, \bar{z}, \bar{t}) &= (u^{(0)}, v^{(0)}, w^{(0)}) \\ &= \left(-\frac{1}{2} \bar{y}^2 \partial_{\bar{z}} \bar{h}, 0, -\frac{1}{2} \bar{y}^2 + \bar{h} \bar{y} \right), \end{aligned} \quad (4b)$$

and at $O(\epsilon)$, the relevant velocity terms for deriving the lubrication model are

$$v^{(1)}(\bar{y}, \theta, \bar{z}, \bar{t}) = -\frac{1}{\widehat{\text{Bo}}} \left(\frac{\bar{y}^2}{2} - \bar{h} \bar{y} \right) \partial_{\theta} (\bar{h} + \bar{\nabla}^2 \bar{h}), \quad (4c)$$

$$\begin{aligned} w^{(1)}(\bar{y}, \theta, \bar{z}, \bar{t}) &= -\frac{1}{\widehat{\text{Bo}}} \left(\frac{\bar{y}^2}{2} - \bar{h} \bar{y} \right) \partial_{\bar{z}} (\bar{h} + \bar{\nabla}^2 \bar{h}) \\ &\quad + \frac{1}{6} (\bar{y}^3 - 3\bar{y}^2 \bar{h} + 3\bar{y} \bar{h}^2). \end{aligned} \quad (4d)$$

Given the choice of scalings (2), the leading order pressure term (4a) represents a balance of the free surface curvature in the radial and axial directions which couples into the velocity field at $O(\epsilon)$ (Eqs. (4c) and (4d)). The leading order axial velocity profile is parabolic due to the gravitational draining of fluid down the cylinder.

To derive the lubrication model, we use conservation of mass with the no-slip and kinematic boundary conditions to obtain the relation

$$(1 + \epsilon \bar{h}) \partial_{\bar{t}} \bar{h} + \partial_{\theta} \bar{Q}_{\theta} + \partial_{\bar{z}} \bar{Q}_{\bar{z}} = 0, \quad (5)$$

where $(1 + \epsilon \bar{h})$ is the scaled radial distance from the cylinder axis to the free surface and the scaled flux components are defined by

$$\bar{Q}_{\theta} = \int_0^{\bar{h}} \bar{v} d\bar{y} = \int_0^{\bar{h}} (v^{(0)} + \epsilon v^{(1)}) d\bar{y} = \frac{\epsilon \bar{h}^3}{3\widehat{\text{Bo}}} \partial_{\theta} (\bar{h} + \bar{\nabla}^2 \bar{h}), \quad (6a)$$

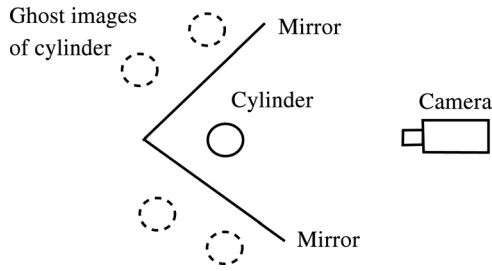


FIG. 2. Schematic of top view of experiment.

$$\begin{aligned}\bar{Q}_z &= \int_0^{\bar{h}} \bar{r}\bar{w} \, d\bar{y} = \int_0^{\bar{h}} (1 + \epsilon\bar{y})(w^{(0)} + \epsilon w^{(1)}) \, d\bar{y} \\ &= \frac{1}{3}(\bar{h}^3 + \epsilon\bar{h}^4) + \frac{\epsilon\bar{h}^3}{3\text{Bo}} \partial_z(\bar{h} + \bar{\nabla}^2\bar{h}).\end{aligned}\quad (6b)$$

Substituting Eq. (6) into Eq. (5) yields an evolution equation for the film height

$$(1 + \epsilon\bar{h})\partial_t\bar{h} + \frac{1}{3}\partial_z(\bar{h}^3 + \epsilon\bar{h}^4) + \frac{\epsilon}{3\text{Bo}}\bar{\nabla} \cdot [\bar{h}^3\bar{\nabla}(\bar{h} + \bar{\nabla}^2\bar{h})] = 0, \quad (7)$$

where $\bar{\nabla} = \mathbf{e}_\theta\partial_\theta + \mathbf{e}_z\partial_z$, the second and third terms represent contributions from gravity and surface tension, respectively, the first two $O(\epsilon)$ terms arise from conserving mass across the cross-sectional area of an annular ring (see Eqs. (5) and (6b)) and the third term arises from the free surface curvature in the radial and axial directions. This model is valid when $\epsilon \ll 1$ and $\epsilon^2\text{Re} \ll 1$. In Sec. IV, we carry out analysis of Eq. (7) by modeling the contact line of the flow with a traveling wave solution and analyzing its linear stability to obtain predictions on the fingering pattern that emerges along the contact line. To simplify notation, the overbar notation is dropped in the rest of the paper.

III. EXPERIMENTS

A. Experimental apparatus and details

To examine the influence of cylinder curvature on fingering behavior, experiments were conducted with six 61 cm

TABLE I. Constant volume experimental details.

Cylinder radius (R) (cm)	Fluid volume (ml)	Reservoir cup inner diameter (cm)	Pressure head (cm)
0.635	5.5	1.10	5.8
0.953	8.5	1.26	6.8
1.27	11	2.19	2.9
3.81	33	6.96	0.9

tall solid, clear cast acrylic cylinders with radii ranging between $0.159 \leq R \leq 3.81$ cm; a top view of the experiment is shown in Fig. 2. Analogous to inclined plane experiments,^{1,2,6,10} the cylinder surface is coated using either a constant volume or constant flux method. For the four largest cylinders ($R \geq 0.635$ cm), a hollow reservoir cup is set directly atop the cylinder and filled with a specific volume of fluid chosen to ensure complete coverage of the cylinder (see Table I); the outer diameter of each reservoir cup matches its companion cylinder and the inner diameter and initial pressure head are listed in Table I. The reservoir cup, which acts as a gate, is raised a height of 1.05 ± 0.02 mm allowing the fluid to flow down the cylinder surface (shown at a later stage in Fig. 3(b)). Capillary effects prevented the experimental fluids, glycerin, and silicone oil, to flow from a reservoir for the two smallest cylinders ($R = 0.159, 0.318$ cm); the capillary length of glycerin and silicone oil are $l_c = 0.22$ cm and 0.15 cm, respectively. For these experiments, a capillary tube (OD = 0.476, 0.636 cm, respectively) connected to a syringe pump is set vertically plumb 1.05 mm above the cylinder, to maintain the same gap height as in the constant volume experiments, and fluid is pumped onto the cylinder at 5 ml/min.

The experimental fluids, 99% weight glycerin (Aldrich) and 1000 cSt silicone oil (Dow Corning), have different wetting properties on acrylic with glycerin partially wetting and silicone oil completely wetting. To distinguish the fluid from the clear cylinder, fluorescent dye (APD Oil and Fluid Dye P/N 801, Corrosion Consultants Inc.) was added to each fluid and the experiment was illuminated with black lights, as shown in Fig. 3(b). Three runs were conducted for every

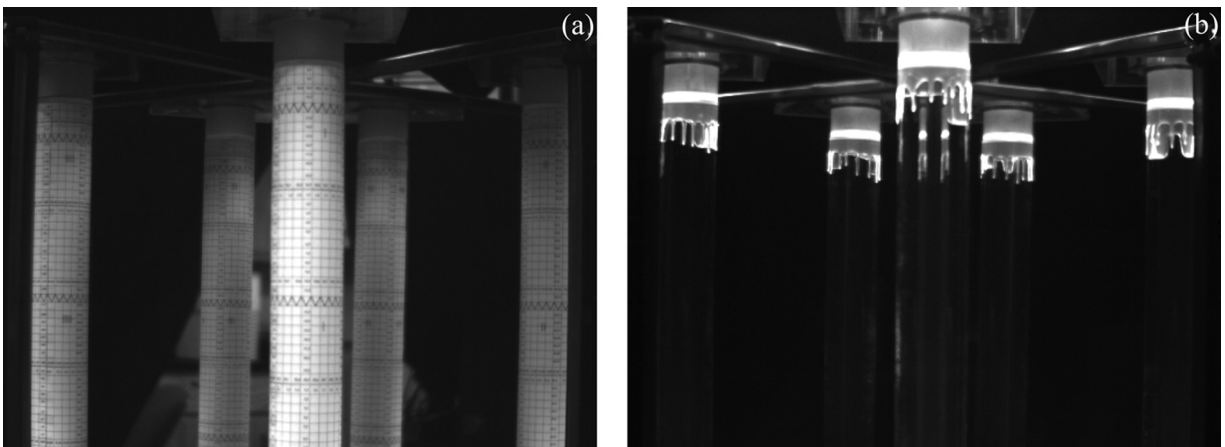


FIG. 3. Experiment: (a) The front of the cylinder is in the center and the two images to the left and right are reflections of the back of the cylinder. (b) Silicone oil fingers develop along the contact line ($R = 3.81$ cm). The fluorescent glow (top center) is the dyed solution remaining in the reservoir.

TABLE II. Experimental details: cylinder radius (cm), slenderness parameter, fluid temperature ($^{\circ}\text{C}$), kinematic viscosity (cm^2/s), Reynolds number, Bond number, and axial distance of contact line at instability (cm).

R	ϵ	Glycerin					Silicone Oil				
		T	ν	Re	$\widehat{\text{Bo}}$	z_p	T	ν	Re	$\widehat{\text{Bo}}$	z_p
0.159	0.533	20.6–21.3	8.46	0.0156	0.536	0.35	~ 21.0	~ 10.6	0.0099	1.12	0.37
0.318	0.266	21.3–21.6	8.18	0.0334	2.14	0.23	21.0	10.6	0.0199	4.46	0.39
0.635	0.133	21.5–21.8	7.98	0.0702	8.55	—	21.5–21.7	10.4	0.0413	17.8	—
0.953	0.0889	20.3–20.4	8.97	0.0833	19.3	0.79	20.2–20.4	10.8	0.0574	40.1	1.46
1.27	0.0667	22.0–22.3	7.71	0.150	34.2	1.08	22.0–22.3	10.3	0.0842	71.2	0.92
3.81	0.0222	21.6–21.8	7.98	0.421	308	0.75	21.8–22.6	10.3	0.252	641	1.21

fluid and cylinder combination; fluid temperatures are reported in Table II. Before each run, the cylinders were washed with Micro cleanser, rinsed with water and ethanol, and dried with a lint-free tissue.

Movies of the flow were recorded at 100 frames/s using a digital imaging camera (Phantom v4.2, Vision Research) with image size 512×384 pixels² and resolution 8 pixels/cm. To visualize around the cylinder periphery, two 61×46 cm² mirrors were placed at an 85.8° angle behind the cylinder (Fig. 2) and the camera was positioned with two reflections of the cylinder appearing in each mirror (Fig. 3). Arc length and axial distances along the cylinder were calibrated with a rectangular grid (Fig. 3(a)) and recorded images were analyzed using software.

In experiments, the contact line loses uniformity close to the cylinder top (the mean axial distance, z_p , is reported in Table II) which made it difficult to measure the upstream film thickness, H , when the contact line initially becomes unstable,²⁷ so instead measurements were made after the instability. After the contact line has moved sufficiently, an equilibrated value of H is estimated as 0.085 ± 0.02 cm with the upper bound equalling the gap height.

Kinematic viscosity was measured using a Brookfield DV-III rheometer; values based on mean fluid temperature are listed in Table II. The surface tension (measured using a Fischer model 21 tensiometer) and density of the glycerin and silicone oil dye solutions are $\gamma = 58.4$ and 21.9 dyn/cm and $\rho = 1.26$ and 0.986 g/cm³, respectively.

The reduced Bond number for glycerin ($\text{Bo} = 0.15$) and silicone oil ($\text{Bo} = 0.32$) are constant in the experiments. The

dimensionless parameters that characterize the flow: the slenderness parameter; Reynolds number; and Bond number, are reported in Table II. In the experiments, $\epsilon \leq O(10^{-1})$ and $\epsilon^2 \text{Re} \leq O(10^{-3})$, which satisfy the conditions of the lubrication model (7) and justifies a comparison between the model and experimental data. For each fluid, ϵ is the only free parameter in Eq. (7) since H is fixed in this study, Bo is constant and $\widehat{\text{Bo}} = \epsilon^{-2} \text{Bo}$.

B. Experimental observations

Perturbations do not form spontaneously along the contact line, as in inclined plane experiments,^{1,9} but rather develop within seconds of each other. Figure 4 shows typical fingering patterns for (a) glycerin and (b) silicone oil. Finger tips and troughs are the maxima and minima downstream axial positions of the contact line. Glycerin fingers form long straight rivulets of nearly uniform width with the tips traveling downstream and the troughs stationary at the cylinder top. The finger shape and behavior of glycerin are identical to observations on an inclined plane.^{1,2,10} Silicone oil fingers are nearly uniform in width downstream from the troughs and the tips and troughs both travel downstream. The finger shape of silicone oil is different than the triangular sawtooth pattern observed on an inclined plane^{1,9} due to the curvature of the cylindrical substrate. In both experiments, the finger length, measured from neighboring tip to trough, and wavelength, measured from neighboring tip to tip, vary across the

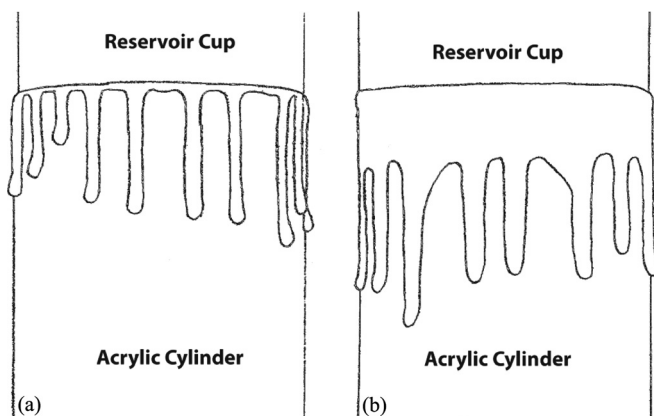


FIG. 4. Typical fingering pattern along cylinder front face for (a) glycerin and (b) silicone oil ($R = 3.81$ cm).

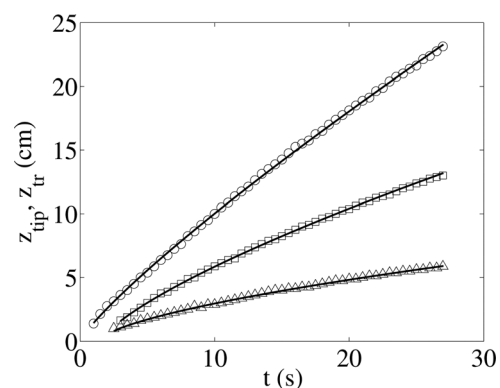


FIG. 5. Downstream tip and trough positions versus time: (○) glycerin tip; (□) silicone oil tip; (△) silicone oil trough (□ and △ are a neighboring tip and trough, $R = 3.81$ cm). Solid curves are best fits to Eq. (8): for glycerin, $z_{\text{tip}} = 1.42(t - 0)^{0.85}$; for silicone oil, $z_{\text{tip}} = 1.22(t - 1.6)^{0.74}$ and $z_{\text{tr}} = 0.75(t - 1.4)^{0.64}$.

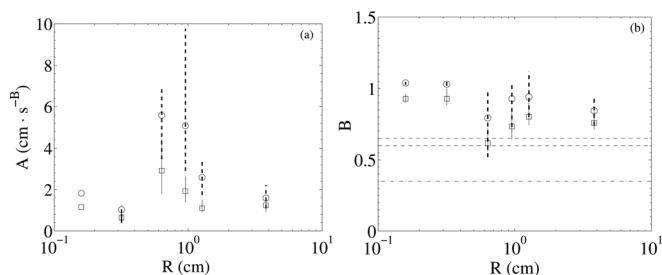


FIG. 6. Amplitude and power from fits of tip positions to Eq. (8) versus cylinder radius for glycerin (\circ) and silicone oil (\square). Symbols denote mean values measured over several fingers and error bars represent range of values. (b) Horizontal lines are data from inclined plane experiments: dashed lines—glycerin ($B=0.60$ (Ref. 1) and $B=0.65$ (Ref. 10)); dotted-dashed line—silicone oil ($B=0.35$ (Ref. 1)).

fingering pattern. In all experiments, the finger tips and non-stationary troughs traveled straight down the cylinder.

The tip (z_{tip}) and trough (z_{tr}) positions in Fig. 5 correspond to a glycerin tip (circles), a silicone oil tip (squares) and a silicone oil trough (triangles) with $R=3.81$ cm; the fluid initially passes the cylinder top at $z=0$ when $t=0$. Best fits of the data (solid curves) are made to the power-law

$$z = A(t - t_0)^B \quad \text{for } t > t_0. \quad (8)$$

Following Ref. 10, tip and trough data for several fingers in three runs were fit to Eq. (8). Values of amplitude A and power B for the six cylinders are shown in Fig. 6 for the tips and in Fig. 7 for the troughs; symbols denote the mean (glycerin—circles and silicone oil—squares) and error bars denote the range of values (glycerin—dashed and silicone oil—solid). Neither A nor B scale with R . In all experiments, finger length ($= z_{\text{tip}} - z_{\text{tr}}$) monotonically increases in time. The horizontal lines in Figs. 6(b) and 7(b) are power data from inclined plane experiments.^{1,10} The cylinder data in Fig. 6 indicates glycerin tips travel faster than silicone oil tips consistent with the behavior in inclined plane experiments.¹ A comparison of power data indicates tip and trough positions travel faster down a vertical cylinder than an inclined plane.

Experimental data of finger width for glycerin (circles) and silicone oil (squares) are shown in Fig. 8 which for convenience is plotted versus \widehat{Bo} ; all fingers were measured in three runs with symbols representing the mean and error bars the standard deviation of the data. Within the standard deviation, finger width is constant at 0.56 cm (dashed line) and

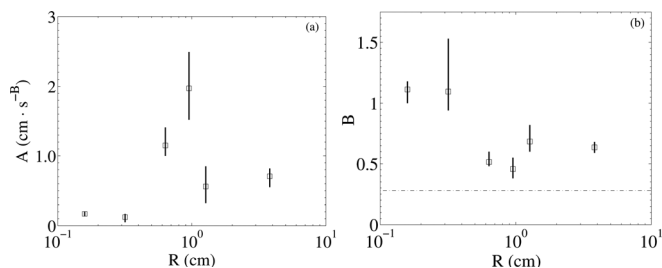


FIG. 7. Amplitude and power from fits of silicone oil trough positions to Eq. (8) versus cylinder radius. Symbols denote mean values measured over several fingers and error bars represent range of values. (b) Dotted-dashed line is data from inclined plane experiments ($B=0.28$ (Ref. 1)).

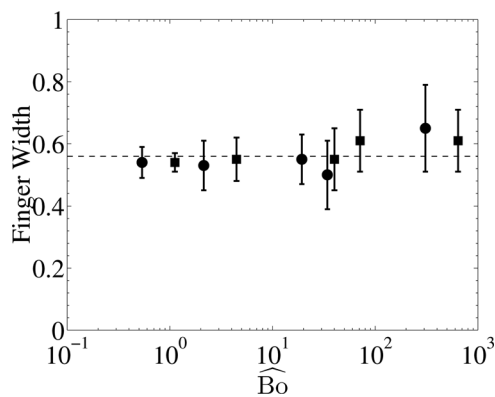


FIG. 8. Finger width versus Bond number measured over several fingers in experiments for glycerin (\bullet) and silicone oil (\blacksquare); symbols—mean value and error bars—standard deviation. Within the standard deviation, finger width is constant at 0.56 cm (dashed line).

thus independent of the wetting conditions, cylinder radii, and flow delivery used in experiments.

The number of fingers that form along a contact line approximates the fingering pattern wave number, q . In experiments, q increases with R ; data from three runs are reported in Table III. Measurements of the mean and standard deviation of finger wavelength, λ , are reported in Table III. The value of λ for the smallest cylinder ($R=0.159$ cm) equals the cylinder circumference since only one finger formed. On average there is a 28% deviation from the mean wavelength in a fingering pattern for $R \geq 0.318$ cm; this is comparable to inclined plane experiments where deviations up to 25% have been reported.^{1,9}

IV. ANALYSIS AND SIMULATIONS

We carry out analysis of the lubrication model (7) by characterizing the unperturbed contact line as an axisymmetric traveling wave solution and examining the stability of the traveling wave using linear analysis. The influence of ϵ and \widehat{Bo} on the traveling wave and its stability is examined, and the stability results are compared to experimental data for q and λ .

A. Traveling wave solution

The base state of the unperturbed flow is an axisymmetric traveling wave solution which under the change of variables $h(z, t) = h_0(\xi)$ in Eq. (7) satisfies

$$-U \left(h_0 + \frac{1}{2} \epsilon h_0^2 \right)' + \frac{1}{3} (h_0^3 + \epsilon h_0^4)' + \frac{\epsilon}{3\widehat{Bo}} (h_0^3 (h_0' + h_0'''))' = 0, \quad (9a)$$

where $\xi = z - Ut$ with traveling wave speed, U . The base state is matched to a flat film upstream of the contact line, $h_0 \rightarrow 1$ as $\xi \rightarrow -\infty$, and to a thin precursor film downstream of the contact line, $h_0 \rightarrow b$ as $\xi \rightarrow +\infty$ with $b \ll 1$.¹⁹ The precursor film prevents a singularity that forms at the contact line on an unwetted surface due to the no-slip condition and has a minimal effect on the stability of the contact line.^{19,20} The value of b cannot be measured in experiments and is a

TABLE III. The number of fingers (q) in a fingering pattern and finger wavelength (λ) measured in experiments and the most unstable wave number (q^*) and most unstable wavelength (λ^*) derived from linear stability theory.

R (cm)	Glycerin				Silicone Oil			
	Experiment q^a (Run 1, 2, 3)	Experiment λ^b (cm)	Theory q^*	Theory λ^{*c} (cm)	Experiment q^a (Run 1, 2, 3)	Experiment λ^b (cm)	Theory q^*	Theory λ^{*c} (cm)
0.159	(1, 1, 1)	1.00	0.74	1.35	(1, 1, 1)	1.00	0.87	1.15
0.318	(2, 2, 2)	1.00 ± 0.09	1.18	1.69	(2, 2, 2)	1.00 ± 0.18	1.47	1.36
0.635	(2, 2, 3)	$\sim 1.77 \pm 0.38$	2.15	1.86	(2, 2, 3)	$\sim 1.77 \pm 0.50$	2.73	1.46
0.953	(3, 3, 4)	1.80 ± 0.95	3.13	1.91	(2, 3, 3)	2.25 ± 0.77	3.99	1.50
1.27	(5, 6, 7)	1.33 ± 0.40	4.12	1.94	(7, 7, 7)	1.14 ± 0.37	5.25	1.52
3.81	(13, 13, 14)	1.80 ± 0.50	12.07	1.98	(16, 18, 18)	1.38 ± 0.43	15.4	1.55

^aNumber of fingers observed in three runs.

^bData averaged over all fingers in three runs.

^cResults from linear stability analysis with $b = 0.07$ and $H = 0.085$ cm.

free parameter in the model. The boundary conditions at $\xi \rightarrow \pm \infty$ sets

$$U = \frac{1 + b + b^2 + \epsilon(1 + b + b^2 + b^3)}{3(1 + \epsilon/2 + \epsilon b/2)}, \quad (9b)$$

and uniquely defines the traveling wave solution, $h_0(\xi)$.

There are standard ordinary differential equation (ODE) methods to solve Eq. (9) numerically.³⁹ Steady-state traveling wave solutions were computed for a range of values of the precursor film thickness ($0.07 \leq b \leq 0.1$) and dimensional upstream film height ($0.065 \leq H \leq 0.105$ cm, taken from experiments). Numerical challenges arise when using smaller values of b on a uniform mesh which restricted the values examined here. In all simulations, the peak of the capillary ridge and steepness of the contact line are decreasing functions of b and H as shown in Figs. 9(a) and 9(b), respectively. Traveling waves moving down a vertical plane have a similar dependence on b .^{8,19,20}

B. Linear stability analysis

For convenience, the lubrication model (7) is transformed to the moving reference frame with $h(\theta, z, t) = \tilde{h}(\theta, \xi, t)$

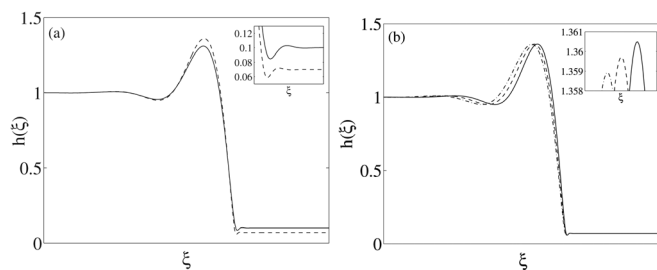


FIG. 9. Influence of (a) precursor film thickness and (b) upstream film height on steady-state traveling wave solutions with $Bo = 0.32$ (corresponding to silicone oil) and $R = 3.81$ cm. In simulations: (a) $b = 0.07$ (dashed), $b = 0.10$ (solid), and $H = 0.085$ cm (inset shows oscillatory decay ahead of contact line); (b) $H = 0.065$ cm (solid), 0.085 cm (dashed), 0.105 cm (dotted-dashed), and $b = 0.07$ (inset shows capillary ridge peaks).

$$\begin{aligned} (\partial_t - U\partial_\xi) \left(\tilde{h} + \frac{\epsilon}{2} \tilde{h}^2 \right) + \frac{1}{3} \partial_\xi (\tilde{h}^3 + \epsilon \tilde{h}^4) \\ + \frac{\epsilon}{3Bo} \left[\partial_\theta (\tilde{h}^3 (\tilde{h}_\theta + \tilde{h}_{\theta\theta} + \tilde{h}_{\xi\xi})) \right. \\ \left. + \partial_\xi (\tilde{h}^3 (\tilde{h}_\xi + \tilde{h}_{\theta\theta\xi} + \tilde{h}_{\xi\xi\xi})) \right] = 0. \end{aligned} \quad (10)$$

After a short period in experiments, the contact line develops an undulatory pattern in θ that grows into a fingering pattern. To model this, the stability of the contact line is examined by superimposing two-dimensional perturbations onto the traveling wave solution with sinusoidal variation in the azimuthal direction

$$\tilde{h}(\theta, \xi, t) = h_0(\xi) + \phi(\xi) e^{\beta t + iq\theta},$$

where $\phi \ll h_0$ and q represents the azimuthal wave number. Substituting \tilde{h} into Eq. (10) and keeping only linear terms in the perturbed variable, ϕ yields the eigenvalue problem

$$\frac{1}{1 + \epsilon h_0} \frac{d}{d\xi} L_0 \phi + \frac{q^2}{1 + \epsilon h_0} L_2 \phi + \frac{q^4}{1 + \epsilon h_0} L_4 \phi = \beta \phi, \quad (11a)$$

with

$$\begin{aligned} L_0 = U(1 + \epsilon h_0) - \frac{1}{3} (3h_0^2 + 4\epsilon h_0^3) \\ - \frac{\epsilon}{3Bo} \left[h_0^3 \left(\frac{d}{d\xi} + \frac{d^3}{d\xi^3} \right) + 3h_0^2 \left(\frac{dh_0}{d\xi} + \frac{d^3 h_0}{d\xi^3} \right) \right], \end{aligned} \quad (11b)$$

$$L_2 = \frac{\epsilon}{3Bo} \left[h_0^3 \frac{d^2}{d\xi^2} + 3h_0^2 \frac{d}{d\xi} \right], \quad (11c)$$

$$L_4 = -\frac{\epsilon}{3Bo} h_0^3, \quad (11d)$$

defined on $\xi \in (-\infty, \infty)$. Solving Eq. (11) numerically first involves computing the traveling wave solution h_0 on the discretized domain $\xi \in [0, L]$. As a result, the corresponding eigenvalue problem involves solving a system of linear equations on $[0, L]$ and appropriate boundary conditions for Eq. (11) must be chosen so that ϕ and its derivatives decay far from the contact line as on an infinite domain. Following Golovin *et al.*,⁴⁰ who examined the linear stability of a thermally driven film with van der Waals forces on a planar

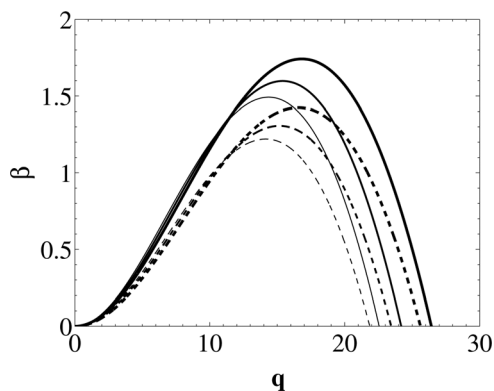


FIG. 10. Dispersion curves of growth rate versus wave number developed from linear stability analysis with $Bo=0.32$ (corresponding to silicone oil) and $R=3.81$ cm. Line types: $b=0.07$ (solid), $b=0.1$ (dashed), $H=0.065$ cm (thick), $H=0.085$ cm (medium), and $H=0.105$ cm (thin).

substrate, this corresponds to the uniform boundary conditions $c_0^{(0)}\phi + c_0^{(1)}\phi_\xi + c_0^{(2)}\phi_{\xi\xi} + \dots = 0$ at $\xi=0$ and $c_L^{(0)}\phi + c_L^{(1)}\phi_\xi + c_L^{(2)}\phi_{\xi\xi} + \dots = 0$ at $\xi=L$ where the coefficients are chosen so that ϕ is minimally affected by the finite domain. The zero eigenmode $\phi = h_{0\xi}$, which arises due to translational invariance, is the most sensitive to the finite domain,⁴⁰ and as a result, the coefficients are chosen so that the zero eigenmode, which behaves like $\phi \sim e^{\lambda\xi}$ as $\xi \rightarrow 0$ and $\xi \rightarrow L$, satisfies the boundary conditions at $\xi=0$

$$\phi_{\xi\xi} - 2\lambda_{0,r}\phi_\xi + (\lambda_{0,r}^2 + \lambda_{0,i}^2)\phi = 0, \quad (12a)$$

$$\phi_{\xi\xi\xi} - 2\lambda_{0,r}\phi_{\xi\xi} + (\lambda_{0,r}^2 + \lambda_{0,i}^2)\phi_\xi = 0, \quad (12b)$$

and $\xi=L$

$$\phi_{\xi\xi} - 2\lambda_{L,r}\phi_\xi + (\lambda_{L,r}^2 + \lambda_{L,i}^2)\phi = 0, \quad (12c)$$

$$\phi_{\xi\xi\xi} - 2\lambda_{L,r}\phi_{\xi\xi} + (\lambda_{L,r}^2 + \lambda_{L,i}^2)\phi_\xi = 0, \quad (12d)$$

where $\lambda_{0,r}$ and $\lambda_{0,i}$ represent the real and imaginary parts of the complex conjugate roots of the characteristic equation coming out of the linearization of the traveling wave solution upstream at $\xi=0$ (corresponding to $h_0=1$) and $\lambda_{L,r}$ and $\lambda_{L,i}$ are likewise defined downstream at $\xi=L$ (corresponding to $h_0=b$). The signs in Eq. (12) have been adjusted from those reported in Golovin *et al.*⁴⁰ (their Eq. (17)). The maximum eigenvalue β of Eq. (11) as a function of q is computed to establish the dispersion relation.

Figure 10 shows dispersion curves illustrating the dependence on precursor film thickness and upstream film height with $b=0.07$ (solid), $b=0.1$ (dashed), $H=0.065$ cm (thick), $H=0.085$ cm (medium), and $H=0.105$ cm (thin). The most unstable wave number (q^*), cutoff wave number for neutral stability (q_{cutoff}), and maximum growth rate (β^*) are decreasing functions of b and H . The value of b has a minor effect on q^* and q_{cutoff} . Using b as a fitting parameter, we set $b=0.07$ since it provides the best comparison between theory and experiments for wave number and wavelength of the fingering pattern. The value of b has a greater influence on β^* , however, experimental data are unavailable to compare to these predictions. Studies analyzing the stabil-

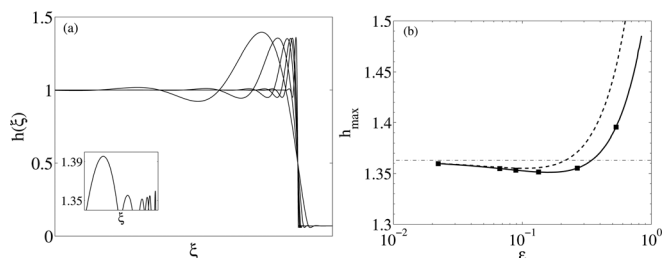


FIG. 11. (a) Traveling wave solutions for silicone oil with $b=0.07$, $H=0.085$ cm, and values of ϵ taken from experiments, $\epsilon = 0.533, 0.266, 0.133, 0.0889, 0.0667, \text{ and } 0.0222$ (left to right). Inset shows capillary ridge peaks. (b) Capillary ridge height versus ϵ for glycerin (dashed) and silicone oil (solid). Squares represent data for traveling waves in (a) and the dotted-dashed line represents h_{max} for a traveling wave down a vertical plane using Eq. (1) with $b=0.07$.

ity of a traveling wave down a vertical plane find that q_{cutoff} and β^* have qualitatively similar dependence on b , while q^* is a weakly increasing function of b .^{8,19,20} The percent difference of q^* , q_{cutoff} , and β^* relative to values with $H=0.085$ cm are 9.3% for $H=0.065$ cm and 6.8% for $H=0.105$ cm. In simulations using experimental parameters (listed in Table II), these percent differences increase with R such that for the smallest cylinder, the percent difference of q^* , q_{cutoff} , and β^* are bounded by 4.6% for $H=0.065$ cm and 4.0% for $H=0.105$ cm. Given the experimental resolution of H , we set $H=0.085$ cm and use the comparisons with $H=0.065$ and 0.105 cm to estimate error bars for q^* , q_{cutoff} , and β^* .

C. Predictions from model and comparison to experiments

Figure 11(a) shows the effect of ϵ , which is proportional to the substrate curvature, on the traveling wave solution with ϵ decreasing (i.e., R increasing) from left to right for the six traveling waves shown; parameters correspond to experiments with silicone oil listed in Table II. As ϵ decreases, the contact line steepens, the capillary ridge width decreases and the capillary ridge height, h_{max} , varies non-monotonically (inset); the first two effects are dramatized since ξ is scaled by R following Eq. (2). For fixed ϵ , the traveling wave solution has a steeper front for silicone oil ($Bo=0.32$) and a wider capillary ridge for glycerin ($Bo=0.15$) (not shown). Figure 11(b) shows the capillary ridge height for glycerin (dashed line) and silicone oil (solid line) as a function of

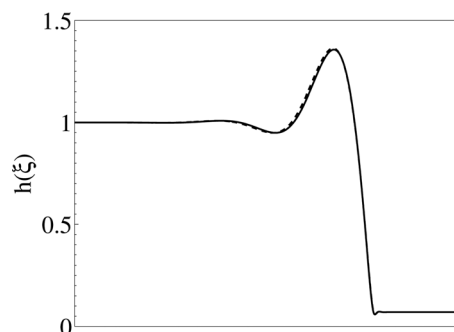


FIG. 12. Traveling wave solutions for glycerin and silicone oil on a vertical cylinder with $\epsilon=0.063$ (solid) and for a vertical plane using Eq. (1) with $b=0.07$ (dashed).

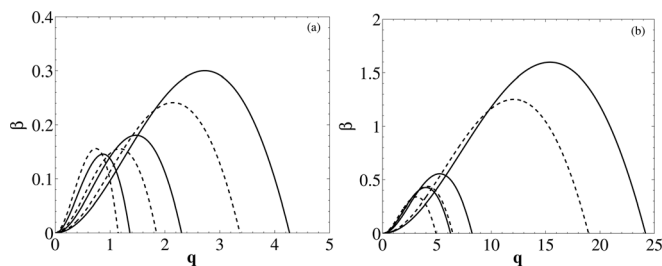


FIG. 13. Dispersion curves for glycerin (dashed, $\text{Bo} = 0.15$) and silicone oil (solid, $\text{Bo} = 0.32$) with $b = 0.07$ and $H = 0.085$ cm. The range of unstable modes is a decreasing function of ϵ for both fluids. (a) $\epsilon = 0.533, 0.266$, and 0.133 ; (b) $\epsilon = 0.0889, 0.0667$, and 0.0222 .

ϵ with squares representing the traveling waves in Fig. 11(a) and the dotted-dashed line corresponding to h_{\max} for a traveling wave down a vertical plane. The influence of curvature on the steady-state traveling wave is negligible when $\epsilon \leq O(10^{-2})$ as the capillary ridge height and shape of the traveling waves converge to the height (Fig. 11(b)) and shape for a vertical plane; an example of the shape is shown in Fig. 12 where the traveling wave solutions for glycerin and silicone oil with $\epsilon = 0.063$ (ζ is rescaled by R/l with $l = (H\gamma/\rho g)^{1/3}$,¹⁹ and $R = 1.35$ cm) are nearly indistinguishable from those down a vertical plane. The substrate curvature has a dominant effect when $\epsilon = O(10^{-1})$ with h_{\max} strongly deviating from the planar value (Fig. 11(b)). Capillary effects also control the capillary ridge height when $\epsilon = O(10^{-1})$ with h_{\max} larger for glycerin ($\text{Bo} = 0.15$) than for silicone oil ($\text{Bo} = 0.32$).

The dispersion curves for glycerin (dashed) and silicone oil (solid) in Fig. 13 indicate the range of unstable wave number is a decreasing function of ϵ for both fluids; values of ϵ are taken from experiments with the three smallest and largest cylinders in Figs. 13(a) and 13(b), respectively. For each cylinder, q^* , q_{cutoff} , and β^* are greater for silicone oil, with the exception of β^* for $\epsilon = 0.533$, indicating the contact line for silicone oil is more unstable to fingering than glycerin for the cylinders examined.

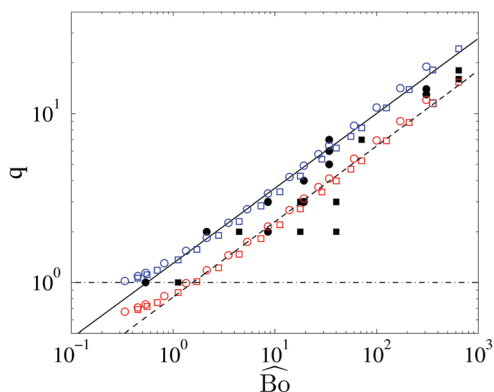


FIG. 14. (Color) Wave number versus Bond number for glycerin (circles) and silicone oil (squares). Solid symbols—experimental data (Table III), blue symbols—cutoff modes, and red symbols—most unstable modes derived from linear stability theory with $b = 0.07$ and $H = 0.085$ cm. Best fits of data: $q_{\text{cutoff}} \sim \widehat{\text{Bo}}^{0.44}$ (solid) and $q^* \sim \widehat{\text{Bo}}^{0.45}$ (dashed). Dotted-dashed line is the critical mode in which one finger grows along the cylinder; the traveling wave solution is stable for $q < 1$. Region of unstable modes is above dotted-dashed line and below solid line.

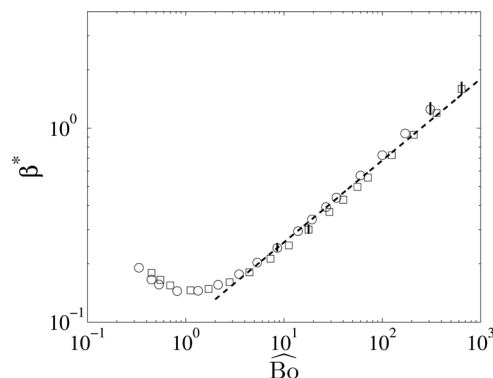


FIG. 15. Maximum growth rate versus Bond number for glycerin (circles) and silicone oil (squares) obtained from linear stability analysis with $b = 0.07$ and $H = 0.085$ cm. Error bars represent range of β^* for $0.065 \leq H \leq 0.105$ cm and dashed line is best fit, $\beta^* \sim \widehat{\text{Bo}}^{0.42}$, for $\widehat{\text{Bo}} \geq 1.3$.

Given the periodicity of the contact line in θ , only an integer number of fingers can form. When nonlinear effects are negligible, finger wavelength is constant and the number of fingers is equivalent to wave number. In this case, the number of fingers observed in experiments should equal the most unstable integer mode predicted from linear stability theory instead of q^* . In experiments, neither the wavelength nor the number of fingers in three runs is constant (see Table III), indicating the contact line is unstable to a range of modes rather than to the fastest growing one. As an approximation, we let the number of fingers represent q in order to compare theoretical predictions to experimental data. One is the fewest number of fingers that can form along the contact line, hence $q = 1$ corresponds to the smallest wave number for fingering. If $q_{\text{cutoff}} < 1$, then in principle, the contact line is stable.

Figure 14 shows a comparison between model and experiments of wave number as a function of Bond number. Experimental data for three runs are denoted by solid symbols with the number of occurrences of q not represented (see Table III for data). Numerical results for q_{cutoff} (blue symbols) and q^* (red symbols) are presented for glycerin (circles) and silicone oil (squares) with the unstable modes represented by the region above $q = 1$ (dotted-dashed line) and below q_{cutoff} (solid line). Agreement is excellent between theory and experiments as data from 32 of 36 runs lie within the region of unstable modes. Considering q is integer-valued in experiments, the comparison is strong for the outlier runs where: (1) $q_{\text{expt}} = 2$ and $q_{\text{cutoff}} = 1.84$; and (2) $q_{\text{expt}} = 7$ and $q_{\text{cutoff}} = 6.46$.

Values of q_{cutoff} and q^* follow the scaling $q_{\text{cutoff}} \sim \widehat{\text{Bo}}^{0.44}$ (solid) and $q^* \sim \widehat{\text{Bo}}^{0.45}$ (dashed) for glycerin and silicone when $\widehat{\text{Bo}} \geq 0.7$ in Fig. 14. These scalings are equivalent to $q_{\text{cutoff}} \sim R^{0.88}$ and $q^* \sim R^{0.9}$, since $\widehat{\text{Bo}} = (R/l_c)^2$, indicating the number of fingers increases approximately linearly with cylinder circumference. These scalings do not apply when $\widehat{\text{Bo}} < 0.7$ corresponding to $\epsilon > 0.47$ for glycerin and $\epsilon > 0.67$ for silicone oil which may represent an upper bound of ϵ that the lubrication model (7) is valid. The stability of the contact line changes when $q_{\text{cutoff}} = 1$, this occurs at $\widehat{\text{Bo}} = 0.56$ corresponding to $\epsilon_c = 0.52$ for glycerin and $\epsilon_c = 0.75$ for silicone oil, such that for $\epsilon \leq \epsilon_c$, the contact

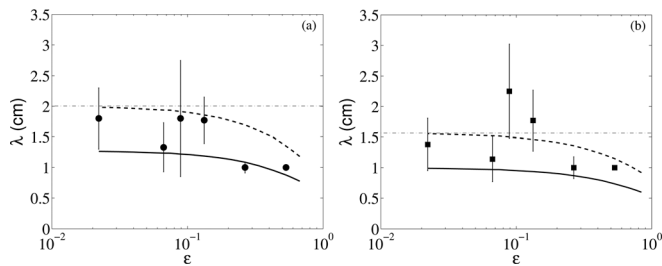


FIG. 16. Finger wavelength versus ϵ for (a) glycerin and (b) silicone oil with most unstable wavelength (dashed) and cutoff wavelength (solid) predicted by stability theory ($b=0.07$ and $H=0.085$ cm). Symbols and error bars represent the mean and standard deviation of experimental data in three runs and dotted-dashed lines represent the most unstable wavelength, $\lambda = 12.6l$, for a traveling wave down a vertical plane (Refs. 19 and 20).

line is unstable to fingering. In principle, the contact line is stable for $\epsilon > \epsilon_c$, though the model may not be valid in this limit. This issue will be addressed in a future analytical study of Eq. (7).

Figure 15 shows maximum growth rate predicted from stability theory versus Bond number for glycerin (circles) and silicone oil (squares) with a sample of error bars displayed. The data follows the scaling $\beta^* \sim \widehat{\text{Bo}}^{0.42}$ (dashed) when $\widehat{\text{Bo}} \geq 1.3$ indicating the instability grows faster as ϵ increases. For $\widehat{\text{Bo}} < 1$, β^* is a decreasing function which explains why β^* is larger for glycerin ($\text{Bo}=0.15$) than silicone oil ($\text{Bo}=0.32$) for the smallest cylinder ($\epsilon = 0.533$) shown in Fig. 13(a).

Figure 16 shows a comparison between model and experiments of finger wavelength as a function of ϵ for (a) glycerin and (b) silicone oil. The solid symbols and error bars represent the mean and standard deviation of the experimental data measured in three runs. The curves represent the most unstable wavelength (dashed), λ^* , and cutoff wavelength for neutral stability (solid), λ_{cutoff} , predicted from stability theory; the contact line is longwave unstable represented by the regions above the solid curves. Agreement is excellent between the model and experimental data.

The model predicts that curvature of the cylindrical substrate has a negligible influence on λ when $\epsilon \leq O(10^{-2})$ as λ_{cutoff} plateaus and λ^* converges to the most unstable wavelength for a contact line down a vertical plane, $\lambda \approx 12.6l$ (value consistent with extrapolating data in Ref. 19 and is a result in Ref. 20) indicated by the dotted-dashed lines in Fig. 16. This represents the same range of ϵ that the capillary ridge height (Fig. 11(b)) and shape of the traveling wave (Fig. 12) converge to the height and shape for a traveling wave down a vertical plane. The substrate curvature has a dominant effect on λ when $\epsilon = O(10^{-1})$ with the range of unstable wavelength an increasing function of ϵ . Capillary effects influence finger wavelength with λ_{cutoff} and λ^* larger for glycerin ($\text{Bo}=0.15$) than for silicone oil ($\text{Bo}=0.32$) as shown in Fig. 16.

V. CONCLUSIONS

This study considers the dynamics of a gravity-driven contact line down the outside of a vertical cylinder. In experiments with glycerin and silicone oil and with cylinder

radii ranging between 0.159 and 3.81 cm, the contact line develops an instability in the azimuthal direction to form a fingering pattern. Glycerin fingers form long straight rivulets of uniform width with stationary troughs at the cylinder top. Silicone oil fingers are nearly uniform in width further downstream from the troughs with tips and troughs both traveling down the cylinder; the finger shape is different than the triangular sawtooth pattern observed down an inclined plane^{1,9} due to the substrate curvature. The fingering patterns are irregular in finger length and wavelength while finger width is constant in all of the experiments.

A lubrication model is derived for a thin viscous film flowing down the outside of a vertical cylinder. The contact line is modeled using a steady-state traveling wave solution and the stability of the traveling wave is examined using linear analysis. The model depends only on $\epsilon = H/R$ for a particular fluid, which is proportional to the curvature of the cylindrical substrate, when the upstream film height H is fixed as in this experimental study. Substrate curvature effects dominate when $\epsilon = O(10^{-1})$, with the capillary ridge height of the traveling wave and range of unstable wavelength of the fingering pattern increasing functions of ϵ . When $\epsilon \leq O(10^{-2})$, the capillary ridge height and shape of the traveling wave and the most unstable wavelength of the fingering pattern converge to the behavior for a fluid front down a vertical plane.

The most unstable wave number, cutoff wave number for neutral stability and maximum growth rate follow the scaling $\widehat{\text{Bo}}^{0.45}$ for $\widehat{\text{Bo}} \geq 1.3$ and the stability of the contact line changes at the critical value $\widehat{\text{Bo}}_c = 0.56$ corresponding to $\epsilon_c = 0.52$ for glycerin and $\epsilon_c = 0.75$ for silicone oil. The contact line is unstable to fingering for $\epsilon \leq \epsilon_c$ and stable for $\epsilon > \epsilon_c$, though the model may not be valid above ϵ_c since $\epsilon \ll 1$ is violated. Modeling the contact line when $H \gtrsim R$ requires either allowing a thicker film relative to the cylinder radius, such as the model proposed by Craster and Matar,³² or including inertial effects, such as the model proposed by Ruyer-Quil *et al.*,³³ which we leave for a future study.

Agreement is excellent between the model and experimental data for the wave number (i.e., number of fingers) and wavelength of the fingering pattern that forms along the contact line for the range of cylinders and fluids examined in this study.

ACKNOWLEDGMENTS

We thank Peko Hosoi, Rachel Levy, Ellen Peterson, Mary Pugh, Michael Shearer, Sandra Troian, and Thomas Witelski for many helpful discussions and Timothy Baker for his aid in building the experimental apparatus. We also thank the reviewers for their valuable comments. This research was supported by the National Science Foundation Grant No. DMS-0707755 and REU Grant No. PHY-0552790 and by the Office of the Provost at Bucknell University.

¹H. E. Huppert, "Flow and instability of a viscous current down a slope," *Nature* **300**, 427 (1982).

²N. Silvi and E. B. Dussan V, "On the rewetting of an inclined solid surface by a liquid," *Phys. Fluids* **28**, 5 (1985).

- ³F. Melo, J. F. Joanny, and S. Fauve, "Fingering instability of spinning drops," *Phys. Rev. Lett.* **63**, 1958 (1989).
- ⁴A. M. Cazabat, F. Heslot, S. M. Troian, and P. Carles, "Fingering instability of thin spreading films driven by temperature gradients," *Nature* **346**, 824 (1990).
- ⁵J. Sur, T. P. Witelski, and R. P. Behringer, "Steady-profile fingering flows in Marangoni driven thin films," *Phys. Rev. Lett.* **93**, 247803 (2004).
- ⁶M. F. G. Johnson, R. A. Schluter, M. J. Miksis, and S. G. Bankoff, "Experimental study of rivulet formation on an inclined plate by fluorescent imaging," *J. Fluid Mech.* **394**, 339 (1999).
- ⁷R. V. Craster and O. K. Matar, "Dynamics and stability of thin liquid films," *Rev. Mod. Phys.* **81**, 1131 (2009).
- ⁸A. L. Bertozzi and M. P. Brenner, "Linear stability and transient growth in driven contact lines," *Phys. Fluids* **9**, 530 (1997).
- ⁹J. R. de Bruyn, "Growth of fingers at a driven three-phase contact line," *Phys. Rev. A* **46**, R4500 (1992).
- ¹⁰J. M. Jerrett and J. R. de Bruyn, "Fingering instability of a gravitationally driven contact line," *Phys. Fluids A* **4**, 234 (1992).
- ¹¹I. Veretennikov, A. Indeikina, and H.-C. Chang, "Front dynamics and fingering of a driven contact line," *J. Fluid Mech.* **373**, 81 (1998).
- ¹²L. M. Hocking, W. R. Debler, and K. E. Cook, "The growth of leading-edge distortions on a viscous sheet," *Phys. Fluids* **11**, 307 (1999).
- ¹³Y. Ye and H.-C. Chang, "A spectral theory for fingering on a prewetted plane," *Phys. Fluids* **11**, 2494 (1999).
- ¹⁴J. Zhou, B. Dupuy, A. L. Bertozzi, and A. E. Hosoi, "Theory for shock dynamics in particle-laden thin films," *Phys. Rev. Lett.* **94**, 117803 (2005).
- ¹⁵J. R. de Bruyn, P. Habdas, and S. Kim, "Fingering instability of a sheet of yield-stress fluid," *Phys. Rev. E* **66**, 031504 (2002).
- ¹⁶O. Pouliquen, J. Delour, and S. B. Savage, "Fingering in granular flows," *Nature* **386**, 816 (1997).
- ¹⁷M. P. Brenner, "Instability mechanism at driven contact lines," *Phys. Rev. E* **47**, 4597 (1993).
- ¹⁸L. W. Schwartz, "Viscous flows down an inclined plane: Instability and finger formation," *Phys. Fluids A* **1**, 443 (1989).
- ¹⁹S. M. Troian, E. Herbolzheimer, S. A. Safran, and J. F. Joanny, "Fingering instabilities of driven spreading films," *Europhys. Lett.* **10**, 25 (1989).
- ²⁰M. A. Spaid and G. M. Homsy, "Stability of Newtonian and viscoelastic dynamic contact lines," *Phys. Fluids* **8**, 460 (1996).
- ²¹L. Kondic and A. L. Bertozzi, "Nonlinear dynamics and transient growth of driven contact lines," *Phys. Fluids* **11**, 3560 (1999).
- ²²D. T. Moyle, M.-S. Chen, and G. M. Homsy, "Nonlinear rivulet dynamics during unstable wetting flows," *Int. J. Multiphase Flow* **25**, 1243 (1999).
- ²³M. H. Eres, L. W. Schwartz, and R. V. Roy, "Fingering phenomena for driven coating films," *Phys. Fluids* **12**, 1278 (2000).
- ²⁴J. A. Diez, L. Kondic, and A. Bertozzi, "Global models for moving contact lines," *Phys. Rev. E* **63**, 011208 (2000).
- ²⁵S. Kalliadasis, "Nonlinear instability of a contact line driven by gravity," *J. Fluid Mech.* **413**, 355 (2000).
- ²⁶L. Kondic and J. Diez, "Pattern formation in the flow of thin films down an incline: Constant flux configuration," *Phys. Fluids* **13**, 3168 (2001).
- ²⁷L. Kondic, "Instabilities in gravity driven flow of thin fluid films," *SIAM Rev.* **45**, 95 (2003).
- ²⁸S. T. Thoroddsen and L. Mahadevan, "Experimental study of coating flows in a partially-filled horizontally rotating cylinder," *Exp. Fluids* **23**, 1 (1997).
- ²⁹A. E. Hosoi and L. Mahadevan, "Axial instability of a free-surface front in a partially filled horizontal rotating cylinder," *Phys. Fluids* **11**, 97 (1999).
- ³⁰P. L. Evans, L. W. Schwartz, and R. V. Roy, "Steady and unsteady solutions for coating flow on a rotating horizontal cylinder: Two-dimensional theoretical and numerical modeling," *Phys. Fluids* **16**, 2742 (2004).
- ³¹I. L. Kliakhandler, S. H. Davis, and S. G. Bankoff, "Viscous beads on vertical fibre," *J. Fluid Mech.* **429**, 381 (2001).
- ³²R. V. Craster and O. K. Matar, "On viscous beads flowing down a vertical fibre," *J. Fluid Mech.* **553**, 85 (2006).
- ³³C. Ruyer-Quil, P. Trevelehan, F. Giorgiutti-Dauphiné, C. Duprat, and S. Kalliadasis, "Modelling film flows down a fibre," *J. Fluid Mech.* **603**, 431 (2008).
- ³⁴L. B. Smolka, J. North, and B. K. Guerra, "Dynamics of free surface perturbations along an annular viscous film," *Phys. Rev. E* **77**, 036301 (2008).
- ³⁵D. Takagi and H. E. Huppert, "Flow and instability of thin films on a cylinder and sphere," *J. Fluid Mech.* **647**, 221 (2010).
- ³⁶C. Huh and L. E. Scriven, "Hydrodynamic model of steady movement of a solid/liquid/fluid contact line," *J. Colloid Interface Sci.* **35**, 85 (1971).
- ³⁷E. B. Dussan V, "The moving contact line: The slip boundary condition," *J. Fluid Mech.* **77**, 665 (1976).
- ³⁸H. P. Greenspan, "On the motion of a small viscous droplet that wets a surface," *J. Fluid Mech.* **84**, 125 (1978).
- ³⁹A. L. Bertozzi, A. Münch, and M. Shearer, "Undercompressive shocks in thin film flows," *Physica D* **134**, 431 (1999).
- ⁴⁰A. A. Golovin, B. Y. Rubinstein, and L. M. Pismen, "Effect of van der Waals interactions on the fingering instability of thermally driven thin wetting films," *Langmuir* **17**, 3930 (2001).